Magnetic ground state of the multiferroic hexagonal $LuFeO_3$

Pittala Suresh,[1] K. Vijaya Laxmi,[1] A. K. Bera,[2] S. M. Yusuf,[2,3] Bheema Lingam Chittari,[4] Jeil Jung,[4] and P. S. Anil Kumar[1,*]

[1]*Department of Physics, Indian Institute of Science, Bangalore 560012, Karnataka, India*

[2]*Solid State Physics Division, Bhabha Atomic Research Centre, Mumbai 400085, India*

[3]*Homi Bhabha National Institute, Anushaktinagar, Mumbai 400094, India*

[4]*Department of Physics, University of Seoul, Seoul 02504, Korea*

(Received 27 November 2017; revised manuscript received 15 March 2018; published 15 May 2018)

The structural, electric, and magnetic properties of bulk hexagonal $LuFeO_3$ are investigated. Single phase hexagonal $LuFeO_3$ has been successfully stabilized in the bulk form without any doping by sol-gel method. The hexagonal crystal structure with $P6_3cm$ space group has been confirmed by x-ray-diffraction, neutron-diffraction, and Raman spectroscopy study at room temperature. Neutron diffraction confirms the hexagonal phase of $LuFeO_3$ persists down to 6 K. Further, the x-ray photoelectron spectroscopy established the 3+ oxidation state of Fe ions. The temperature-dependent magnetic dc susceptibility, specific heat, and neutron-diffraction studies confirm an antiferromagnetic ordering below the Néel temperature (T_N) $\sim$ 130 K. Analysis of magnetic neutron-diffraction patterns reveals an in-plane (ab-plane) 120° antiferromagnetic structure, characterized by a propagation vector $k = (0\,0\,0)$ with an ordered moment of 2.84 μ_B/Fe^{3+} at 6 K. The 120° antifferomagnetic ordering is further confirmed by spin-orbit coupling density functional theory calculations. The on-site coulomb interaction (U) and Hund's parameter (J_H) on Fe atoms reproduced the neutron-diffraction Γ_1 spin pattern among the Fe atoms. P-E loop measurements at room temperature confirm an intrinsic ferroelectricity of the sample with remnant polarization $P_r \sim 0.18\,\mu C/cm^2$. A clear anomaly in the dielectric data is observed at $\sim T_N$ revealing the presence of magnetoelectric coupling. A change in the lattice constants at T_N has also been found, indicating the presence of a strong magnetoelastic coupling. Thus a coupling between lattice, electric, and magnetic degrees of freedom is established in bulk hexagonal $LuFeO_3$.

DOI: 10.1103/PhysRevB.97.184419

I. INTRODUCTION

Multiferroic materials are of great interest in recent times due to their technological and scientific importance. They are fascinating due to the coexistence of electric and magnetic orders, simultaneously. The mutual control of charge and spin orders leads to a new effect called magnetoelectric (ME) coupling, due to which these materials are very promising candidates for applications in memory devices and sensors [1–3]. However, it is very rare to find multiferroics having a finite ME coupling at room temperature (RT). To date, $BiFeO_3$ (BFO) perhaps is the only RT multiferroic having coupling between spin and charge orders. However, the ME effect is relatively weak in this material due to its cycloid spin structure [4]. Thus, the quest is immense in the research community for (i) finding new multiferroic compounds and (ii) improving the ME coupling coefficient of the existing multiferroics at RT. Other than BFO, rare-earth manganites, $RMnO_3$ (R = La–Lu, Y, or Sc), are the most meticulously studied multiferroic systems [5]. $RMnO_3$ compounds can have favorable crystallization in both orthorhombic and hexagonal phases depending on the choice of the rare-earth element. The orthorhombic structure (o-$RMnO_3$) with $Pbnm$ symmetry is possible for large R ionic radius (R = La–Dy) while the hexagonal structure (h-$RMnO_3$) with $P6_3cm$ symmetry is possible for small R ionic radius (R = Ho–Lu, Y, or Sc) [6–10]. Despite the room-temperature antiferromagnetism (AFM) exhibited by orthorhombic $RMnO_3$, these materials have very weak polarization, which is induced by its magnetic structure, thus hinders the observation of ME coupling. Nevertheless, hexagonal manganites are fascinating due to their noncentrosymmetry, which leads to high polarization and high ferroelectric (FE) transition temperature [$T_C \sim 900$ K] [11,12]. In these systems, the ferroelectricity mainly originated from the polar $P6_3cm$ crystal structure [9] while the ME coupling is mediated by magnetoelastic coupling [13]. However, the magnetic order in these systems appears at temperatures much lower than RT (∼below 100 K) [9,14,15], and Mn spins couple feebly with its FE order due to its antiferromagnetism. The magnetic ordering is expected to be higher in the isostructural hexagonal ferrites (h-$RFeO_3$, R = Ho–Lu, Y, or Sc), due to (i) the strong exchange coupling between Fe^{3+} ions in the lattice compared with Mn^{3+} ions [16] and (ii) the high localized magnetic moment of Fe [12]. Hence, h-$RFeO_3$ systems are expected to exhibit higher magnetization and ordering temperature, which is essential for practical device applications. Conversely, unlike manganites, $RFeO_3$ compounds tend to exhibit orthorhombic structure for all the rare-earth elements [8].

Hexagonal $LuFeO_3$ (h-$LuFeO_3$) has attracted immense interest due to the theoretical prediction of reversal of magnetization along the c axis using an external electric field [12]. These theoretical calculations are performed by considering the Γ_2 spin configuration of the h-$LuFeO_3$ which allows

*Corresponding author: anil@physics.iisc.ernet.in

the ferromagnetism (FM) in the material. A very recent article by Wang *et al.* [17] based on experimental thin-film work claimed h-$LuFeO_3$ as a room-temperature multiferroic compound. They have reported Γ_2 spin configuration with a high-temperature magnetic transition, T_N, at 440 K, which is highly debated. A later study by Disseler *et al.* [18] argued that the actual T_N of this material is below 150 K with Γ_1 spin configuration, which allows complete AFM, and stated that the 440-K transition observed by Wang *et al.* [17] corresponds to a structural transition. Thus, the ambiguity on the magnetic ordering temperature and the nature of spin configuration of h-$LuFeO_3$ is resolved in thin films. But, no studies are found on bulk or single-crystal samples. Moreover, the spin frustration due to the triangular spin arrangement on the hexagonal lattice of h-$LuFeO_3$ promotes the instability of the magnetic structure and leads to rich magnetic phase diagrams [19]. Therefore, it is essential to study the multiferroic nature of single phase h-$LuFeO_3$.

In order to investigate the magnetic ordering and to understand the underlying mechanism, bulk samples, free of external influences, are essential [20,21]. However, the preparation of single phase h-$LuFeO_3$ is very challenging in the bulk form due to its metastable nature, and often ends up being in the orthorhombic *Pbnm* phase [22,23]. Nevertheless, the hexagonal phase is stabilized in thin-film form by using epitaxial strain [17,18,24]. Thus, the studies on h-$LuFeO_3$ so far are limited to the thin films [8,17,18,24–26]. In literature, a few reports can be traced on the synthesis of h-$LuFeO_3$ in bulk form [27–29]. But, no electric or magnetic studies are reported on the bulk single phase h-$LuFeO_3$ system. Kumar *et al.* [27,28] obtained the h-$LuFeO_3$ minor phase as an impurity in the o-$LuFeO_3$ major phase through quenching high-temperature melt rapidly. The hexagonal phase of $LuFeO_3$ can be stabilized in the bulk form by a doping method; either at the Lu site or at the Fe site by suitable ions [20,21,30]. Disseler *et al.* [20] studied the $LuFeO_3$ with Sc doped at the Lu site and Mn doped at the Fe site to stabilize the hexagonal structure. Lin *et al.* [21] and Masuno *et al.* [30] doped Sc at the Lu site and stabilized the hexagonal phase.

In spite of these reports, pure h-$LuFeO_3$ bulk studies are highly desirable to understand and investigate its electric and magnetic ordering temperatures. This material is not only promising in technological applications but, more importantly, is extremely intriguing for fundamental research. Detailed study of the structure and ferroelectric behavior is essential to have a comprehensive understanding of this new h-$RFeO_3$ multiferroic material. In the present paper we aimed to (i) synthesize hexagonal $LuFeO_3$ in bulk form, (ii) investigate the detailed magnetic ordering, (iii) explore the crystal structure as a function of temperature, and (iv) explore possible coupling between crystal, electric, and magnetic orders. Keeping these goals in mind, we have successfully stabilized the hexagonal single phase in the $LuFeO_3$ bulk ceramics using optimized sol-gel synthesis conditions; the sample quality is confirmed by Raman and x-ray photoemission spectroscopy (XPS) studies. By using neutron and magnetometer studies, we have shown that single phase h-$LuFeO_3$ orders antiferromagnetically below 130 K with the moment lying in the ab plane. P-E loop measurements confirm a spontaneous polarization at room temperature. A comprehensive temperature-dependent study by magnetization, specific heat, dielectric constant, and neutron diffraction reveals coupling between the crystal structure and magnetic and electric orders, proving the magnetoelectric coupling in h-$LuFeO_3$ multiferroic material. Our experimental findings are suppoted by density functional theory (DFT) calculations.

II. EXPERIMENTS

A. Experimental details

High-purity chemicals, $Lu(NO_3)_3 \cdot H_2O$ (99.9%, Alfa Make) and $Fe(NO_3)_3$ $9H_2O$ (99.9%, Alfa Make), were taken as precursors for the preparation of lutetium ferrite using the sol-gel method. These powders were carefully weighed stoichiometrically in 1:1 molar ratio and dissolved separately in 20 ml of 1:5 dil. HNO_3 solution. These solutions were stirred continuously for 5 h under magnetic stirrer. Once the solution became completely transparent, these two solutions were mixed in a beaker and citric acid was added as a chelating agent under the constant stirring at room temperature. This mixture was stirred for 4 to 5 h to form a highly uniform solution. Finally, the solution was heated at 250 °C constant temperature using a hot plate. The brown color fumes evolve from the solution, and at the end of the reaction the formation of the gel was observed. The xerogel powder obtained in the above process was ground finely using agate mortar. Finally, to obtain the crystal structure, these powders were calcinated at 750 °C for 10 h. The calcinated powders were pressed into pellets of 10-mm diameter and annealed for the densification. These densified samples were used for the further characterization.

Structure and purity of the $LuFeO_3$ powder were examined by a Smart Lab x-ray diffractometer with the Cu-K_α source ($\lambda = 1.5418$ Å). High-resolution XPS data were collected using a Kratos Axis Ultra X-ray Photoelectron Spectrometer, model AXIS 165 equipped with an ion gun (EX-05) for cleaning the surface. Binding-energy resolution was 0.01 eV, while background correction was done by using the Shirley algorithm and data were fitted using the Casa XPS Spectroscopy software. The core-level binding energies were aligned with the carbon binding energy of 284.5 eV. Vibrational modes of the sample were examined by the Horiba JobinYvon, LabRAM-HR 800 micro-Raman system equipped with an excitation wavelength of 514.5 nm and laser power of 3 mW under backscattering geometry using a 50X objective lens. For electrical measurements, silver electrodes were made on both sides of the sample disc to make capacitor geometry. Dielectric constant measurements were carried out using an Agilent E4980A LCR meter at different frequencies. Ferroelectric measurements were performed at room temperature using the Radiant precision premier II. Field- and temperature-dependent magnetic measurements were performed on a Quantum Design superconducting quantum interference device magnetometer. Neutron-diffraction patterns were recorded by using the powder diffractometers PD-I ($\lambda = 1.094$ Å) and PD-II ($\lambda = 1.2443$ Å) at Dhruva reactor, Trombay, India. The limited Q-range powder diffractometer PD-I was used to study the temperature evolution of the magnetic Bragg peaks with higher statistics. For the neutron-diffraction measurements, samples were filled in a vanadium can of diameter 5 mm. All

low-temperature measurements were performed by using a closed cycle helium refrigerator. The neutron-diffraction patterns were analyzed by the Rietveld method by using the FULLPROF suite computer program [31].

B. Results and discussion

The crystal structure of $LuFeO_3$ is investigated by both x-ray and neutron-diffraction techniques. In general, bulk $LuFeO_3$ is known to exist in the orthorhombic structure. It is hard to stabilize the hexagonal structure of $LuFeO_3$ in the bulk form compared to thin films. The powders are calcinated at different temperatures from 750 to 900 °C. It is observed that the calcination temperature plays a key role in stabilizing the hexagonal phase. The metastable single phase hexagonal structure was obtained for the samples calcined at 750 °C. Further, as the calcination temperature increases, the orthorhombic phase grows and a single phase orthorhombic with *Pbnm* space group is found for the samples calcined at 900 °C. That means, as the temperature increases, the hexagonal phase transforms to the orthorhombic phase, which is thermodynamically stable at high calcination temperature. Therefore, in the present paper, single phase *h*-$LuFeO_3$ is prepared by controlling the calcination temperature. The x-ray diffraction (XRD) and neutron-diffraction patterns of $LuFeO_3$ recorded at 300 K are depicted in Figs. 1(a) and 1(b). Refinements were performed for both the hexagonal and orthorhombic structural phases. An agreement between observed and calculated patterns is obtained for the hexagonal phase. The refinements confirm that our sample crystallizes in the hexagonal structure with noncentrosymmetric space group $P6_3cm$. The refined values of lattice parameters are $a = b = 5.9430(4)$ Å, $c = 11.7108(11)$ Å, $\alpha = \beta = 90°$, $\gamma = 120°$, and cell volume $V = 358.21(5)$ Å^3 at RT (Table I). The crystal structure of the *h*-$LuFeO_3$ has a rotational symmetry at RT. A schematic representation of the hexagonal crystal structure is shown in Fig. 1(c); the structure cartoon was prepared by using the VESTA software [32]. It is observed that each unit cell consists of two layers of Fe-O and Lu-O each. Within the unit cell, Lu atoms are situated at two crystallographic sites (Lu1:2*a* and Lu2:4*b* sites), Fe is situated at the 6*c* site, and oxygen atoms are situated at four crystallographic sites (O1 and O2, 6*c*; O3, 2*a*; O4, 4*b*). Each Fe atom is surrounded by five oxygen atoms forming a FeO_5 trigonal bipyramid, while the Lu atom is surrounded by eight oxygen atoms forming a LuO_8 cage. There is a presence of slight rotation of the FeO_5 trigonal bipyramids along the [1 0 2] crystal axis. The rotation in the FeO_5 breaks the inversion symmetry and allows ferroelectricity along the *c* axis in this compound [23]. It is found that the FeO_5 trigonal bipyramids are distorted where the Fe ions shift from the center of the FeO_5 towards O_4 (one of the equatorial oxygens) leading to a removal of threefold as well as twofold rotation symmetry. Along the *c* axis, two bond lengths are also found to be unequal, where the bond length Fe-O1 = 1.9361(2) Å is shorter than the bond length Fe-O2 = 1.9772(2) Å (Table II). Moreover, a tilting of the FeO_5 trigonal bipyramid with respect to the *c* axis is evident with an angle between the O1-Fe-O2 direction and the *c* axis of ~4.29(9) Å. On the other hand, unequal bond lengths are also evident for LuO_8 polyhedra where Lu1-O3 distance,

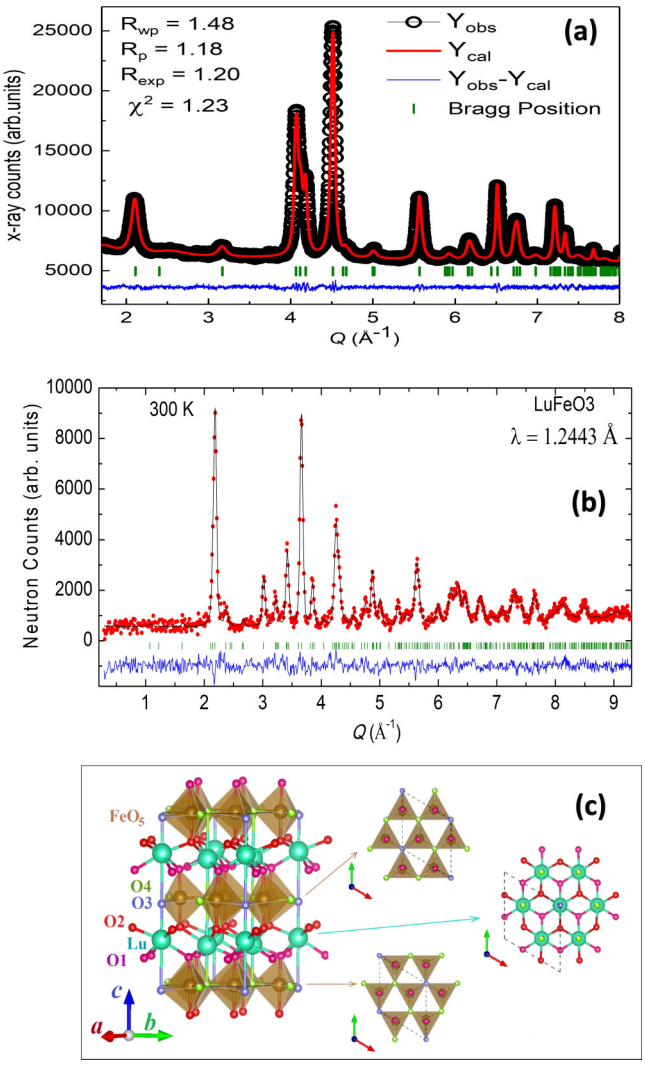

FIG. 1. Rietveld refined (a) x-ray and (b) neutron-diffraction patterns at 300 K. The observed and calculated patterns are shown by circles and lines, respectively. The difference between the observed and calculated patterns is shown by the blue line at the bottom of each panel. The vertical bars represent the Bragg peak positions. (c) The unit cell of *h*-$LuFeO_3$ shown with FeO_5 polyhedra cages. The arrangements of the FeO_5 octahedra at $z = 0$ and $\frac{1}{2}$ layers and Lu atoms within the *ab* layers are also shown.

2.4597(3) Å, is shorter than the Lu2-O4 distance, 2.7031(3) Å, along the *c* axis, which is the polar direction of this material. It is also found that the Lu atoms have an asymmetric vertical shift with respect to the neighboring oxygen atoms along the *c* axis, which results in a noncentrosymmetry and, hence, the observation of ferroelectricity in *h*-$LuFeO_3$ [25,33].

The room-temperature Raman spectrum of polycrystalline *h*-$LuFeO_3$ is depicted in Fig. 2. Besides XRD, Raman spectroscopy is another powerful tool to investigate the crystal purity and crystal symmetry of the samples [34]. Active Raman modes for the *h*-$LuFeO_3$ in its polar $P6_3cm$ symmetry can be represented as [35–37]

$$\Gamma_{P6_3cm} = 9A + 14E_1 + 15E_2.$$

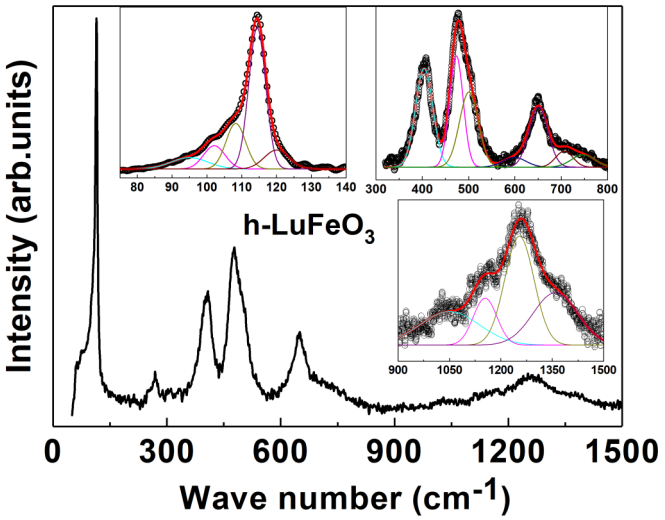

FIG. 2. The measured Raman spectra of h-$LuFeO_3$ at RT. The inset images show the fitted spectra for different ranges (red line).

Hexagonal $LuFeO_3$ with $P6_3cm$ symmetry contains six formula units per unit cell, which make 38 possible Raman active modes [18]. There are in total 19 prominent active Raman modes observed experimentally (after deconvolution) in the present paper. The Raman peak positions are in good agreement with the previous reports on the h-$LuFeO_3$ thin films [18]. It is also noted that the observed Raman modes are considerably different from those expected for orthorhombic $LuFeO_3$ [38], clearly confirming that the $LuFeO_3$ sample under study is in the polar hexagonal phase.

In order to confirm the valence states of the Lu and Fe, the XPS measurements are performed at RT. Figure 3 shows the observed peak positions for the Fe $2p$ and Lu $4f$ spectra of h-$LuFeO_3$. It is observed that Fe has two prominent peaks at ~710.2 and ~723.9 eV corresponding to Fe^{3+} $2p3/2$ and $2p1/2$ states [39]. In addition to these peaks, a small satellite peak at ~718.2 eV is also noticed. XPS spectra of Fe $2p$ along with the associated satellite peak are characteristics of the Fe^{3+} valence state, which is consistent with the values reported for Fe^{3+} [39–42].

Figure 4(a) shows the field cooled (FC) and zero-field cooled (ZFC) magnetization-temperature (M-T) curves of h-$LuFeO_3$ in the temperature range 3 to 400 K under 100-Oe applied magnetic field. From Fig. 4, a hump is seen around 130 K, which is associated to the antiferromagnetic Néel transition, T_N. Below this temperature, unlike the typical AFM, a slight increase in the magnetization is found, due to a possible canting of AFM spins. The magnetic ordering in the hexagonal phase of $LuFeO_3$ is highly discussed. So far, there are no experimental works on the single phase h-$LuFeO_3$ bulk samples. Based on $LuFeO_3$ thin films, Wang *et al.* [17] reported a magnetic ordering around 440 K associated with a spin reorientation at around 120 K. In contrast, Disseler *et al.* [18] proved that the transition observed by Wang *et al.* [17] at 440 K is not the true magnetic order of h- $LuFeO_3$ but related to a structural phase transition from the nonpolar $P\bar{3}c$ to the polar $P6_3cm$ structure. Disseler *et al.* [18] reported that the spins lie in the canted antiferromagnetic order below 150 K for all the h-$LuFeO_3$ films grown on different substrates. The magnetic transition for most of the doped bulk h-$LuFeO_3$ ceramics is reported to be below room temperature [20,43]. However, a high-temperature magnetic transition above 425 K is observed in the case of Sc-doped $LuFeO_3$ samples [21]. Nevertheless, the nature of this particular high-temperature magnetic transition remains debatable, whether it is intrinsic to the h-$LuFeO_3$ system or related to a structural phase transition. In the present paper, we do not see any magnetic transition above 130 K within the measurement range up to 550 K (see Supplemental Material, Fig. S1 [44]), having paramagnetic behavior. The observed $T_N \sim 130$ K for the present compound is also supported by theoretical estimation which predicts that to achieve room-temperature multiferroicity in the h-$RFeO_3$ compounds the c/a ratio should be greater than 2.15 [20]. The c/a ratio of the present compound is 1.97, which suggests the T_N should be below room temperature. The magnetic transition temperature ($T_N \sim 130$ K) of h-$LuFeO_3$ is higher than that of the isostructural compounds $LuMnO_3$ ($T_N \sim 92$ K) and $LuMn_{0.5}Fe_{0.5}O_3$ ($T_N \sim 112$ K) [20,21,45,46]. The magnetic order is primarily dominated by antiferromagnetic Fe-O-Fe superexchange and is complemented by Fe-O-O-Fe super-superexchange in the stacked triangular lattice [47]. The higher magnetic ordering temperature of h-$LuFeO_3$ reveals a stronger

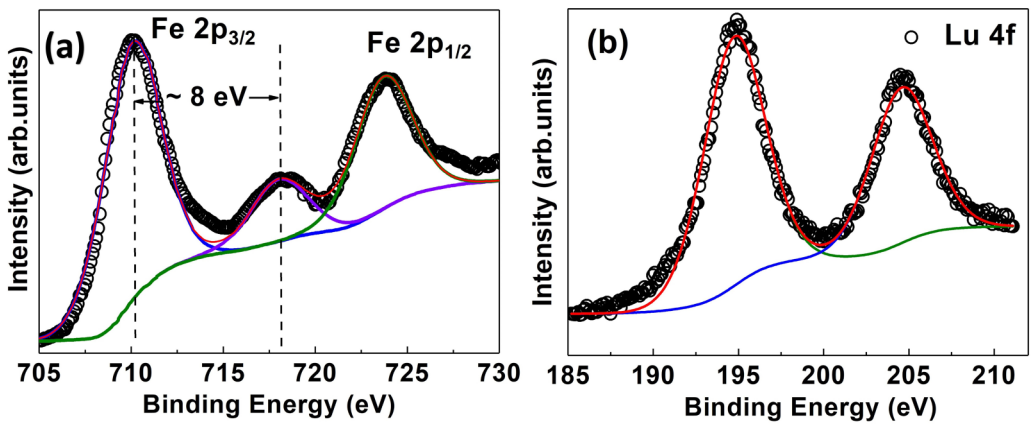

FIG. 3. XPS spectra of (a) Fe $2p$ peaks and (b) Lu $4f$ peaks of h-$LuFeO_3$.

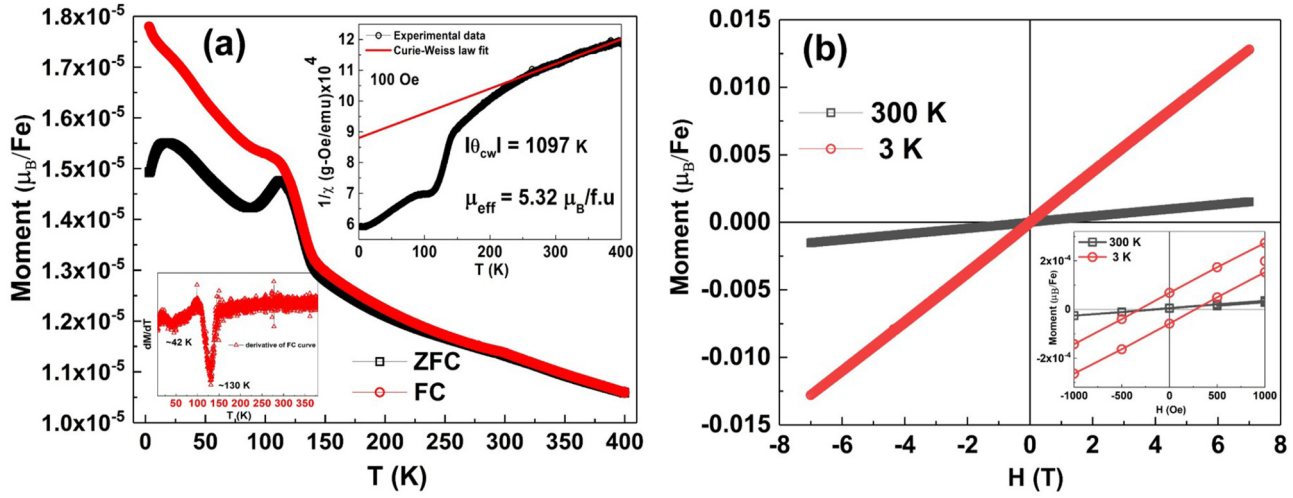

FIG. 4. (a). The ZFC and FC curves of h-$LuFeO_3$ under 100-Oe applied field. The inset shows the FC derivative curve, inverse susceptibility plot of the FC curve, and Curie-Weiss law fitting. (b). M-H curves of the h-$LuFeO_3$ at 3 and 300 K (the inset shows the zoomed part near the origin for the same plot).

exchange interaction as compared to $LuMnO_3$ because Fe^{3+} possesses one more unpaired electron than Mn^{3+}. Besides the onset of magnetic ordering at T_N, another anomaly at $T \sim 42$ K is also evident in the M-T curve. Similar findings are reported in earlier studies on $LuMn_{0.5}Fe_{0.5}O_3$ and $LuMn_{0.7}Fe_{0.3}O_3$ samples at around ~55 K [43,46], which is attributed to the spin-reorientation temperature.

The inverse magnetic susceptibility ($1/\chi$) of h-$LuFeO_3$ at 100 Oe is shown in the inset of Fig. 4(a). Curie-Weiss–like temperature dependence $\chi(T) = C/(T - \theta)$ with a Curie constant C and a Curie-Weiss temperature θ is observed. At high temperatures (above 200 K), the $1/\chi$ (T) curve follows the Curie-Weiss law with a negative Weiss temperature (θ). This indicates the presence of a predominant AFM coupling among Fe-Fe spins and the estimated $|\theta|$ from the fit is 1097 K, the Curie constant is 0.0127 $cm^3\,g^{-1}$ K, and the effective magnetic moment is 5.32 μ_B/f.u. The value of the θ is higher compared to that for the undoped $LuMnO_3$, which is ~820 K [46]. The recent findings show that the T_N and $|\theta|$ increase with an increase of Fe content in $LuMnO_3$ [43], which is consistent with our findings on undoped $LuFeO_3$. The increase in Néel and Weiss temperatures is due to the increase in exchange interactions between magnetic Fe ions within the ab planes as the lattice constant decreases with Fe concentration [47]. The calculated frustration parameter for h-$LuFeO_3$ is 8.43, classifying this spin system as a strong geometrically frustrated system [43].

Field-dependent magnetization (M versus H) curves are measured at 3 and 300 K by sweeping the 7-T external field and shown in Fig. 4(b). At 300 K, the M-H curve shows a typical paramagnetic behavior with a linear curve having zero magnetic remanence and coercivity (H_C), whereas the M-H curve at 3 K shows a slight opening in the loop resulting in $H_C = 290$ Oe. However, the loop still lacks the tendency of saturation, suggesting a weak ferromagneticlike behavior. The magnetization value at 7 T (M_{7T}) increases from 0.0015 μ_B/Fe to 0.013 μ_B/Fe as the temperature decreases from 300 to 3 K, however M_{7T} remains very weak. These findings are in agreement with the M-T observations. The observed low-temperature hysteresis loop at 3 K may be arising from a Dzyaloshinskii-Moriya interaction by the nonperfect triangular arrangement of Fe ions in the ab plane [20]. A nonperfect triangular arrangement of Fe ions for the present compound is evident from the deviation of the c/a value [0.3276(35)] from an ideal value of 1/3 (Table I).

Further, to get more insight on the crystal structure and magnetic ground state, neutron-diffraction measurements are performed over the temperature range 3 to 300 K. The crystal structure for $LuFeO_3$ is found to be hexagonal over the studied temperature range. The temperature-dependent neutron-diffraction patterns are shown in Fig. 5. From Fig. 5, it is found that, with decreasing temperature, additional magnetic Bragg peaks are found below $T_C \sim 130$ K. Upon further lowering of temperature, a monotonous increase in the intensity of the magnetic Bragg peaks is observed without any change in their Q (magnitude of scattering vector) position. This confirms that there is no change of magnetic propagation vector over the measured temperature range. This also implies that the magnetic structure remains unchanged over the studied temperature range. Though the M-T measurements show an anomaly at around ~42 K [inset of Fig. 4(a)], neutron experiments do not show any signature of spin reorientation at this temperature, as it would lead to a certain change of intensity of the (1 0 0) magnetic Bragg peak. In the previous studies on $LuMnO_3$, the spin reorientation transition is observed in the optical experiments while it is absent in neutron scattering [9]. On the other hand, the $ScMnO_3$ sample exhibits spin reorientation in the neutron studies [9]. It is not very clear why neutron experiments have not shown any sign of spin reorientation in a few samples. Nevertheless, the previous works on h-$LuFeO_3$ thin films [18] show spin reorientation transition in the neutron measurements for different samples grown on YSZ-250 and Al_2O_3-200 nm, where they observe a decrease in the intensity of (1 0 0) reflection to zero above the spin reorientation transition (53 K for YSZ-250 nm and 38 K for Al_2O_3-200 nm). However, the thin-film samples grown on YSZ-200- or

TABLE I. The Rietveld refined lattice constants (a and c), fractional atomic coordinates, and isotropic thermal parameters (B_{iso}) for h-$LuFeO_3$ at 300 and 6 K, and the DFT (spin-orbit with non-collinear spins along with $U = 4.5$ eV and $J_H = 0.95$ eV) optimized parameters (described later) are given in the curly brackets for comparison. [300 K ($P6_3cm$): R_p: 3.03% R_{wp}: 3.79% R_{exp}: 1.75% χ^2: 4.70%] and [6 K ($P6_3cm$): R_p: 3.41% R_{wp}: 4.21% R_{exp}: 1.78% χ^2: 5.62% R_{mag}: 16.0%].

300 K ($P6_3cm$)				
$a = 5.9430(4)$ {5.8833} Å; $c = 11.7108(11)$ {11.7077} Å; $V = 358.21(5)$ {350.97} Å^3				
Atom	x/a	y/b	z/c	B_{iso} (Å^2)
Lu1	0	0	0.2665(32) {0.27473}	0.38(8)
Lu2	1/3	2/3	0.2315(21) {0.22477}	0.38(8)
Fe	0.3276(35) {0.33398}	0	0	0.68(5)
O1	0.3083(43) {0.29448}	0	0.1649(21) {0.15965}	1.08(8)
O2	06595(47) {0.62773}	0	0.3313(19) {0.33188}	1.08(8)
O3	0	0	0.4765(40) {0.46901}	1.08(8)
O4	1/3	2/3	0.0069(34) {0.01913}	1.08(8)
6 K ($P6_3cm$)				
$a = 5.9365(4)$ {5.9417} Å; $c = 11.7106(12)$ {11.7209} Å; $V = 357.30(8)$ {358.36} Å^3				
Lu1	0	0	0.2655(36){0.27584}	0.16(6)
Lu2	1/3	2/3	0.2301(18){0.22789}	0.16(6)
Fe	0.3266(39){0.33379}	0	0	0.57(4)
O1	0.2924(46){0.29648}	0	0.1650(26){0.16222}	0.67(7)
O2	06698(43){0.62957}	0	0.3319(21){0.33363}	0.67(7)
O3	0	0	0.4840(36){0.47109}	0.67(7)
O4	1/3	2/3	0.0114(37){0.02072}	0.67(7)

Al_2O_3-200-nm samples have the finite intensity of (1 0 0) reflection till the magnetic transition, indicating the absence of spin reorientation signature in neutron data [18]. Likewise, the present studies on the hexagonal $LuFeO_3$ bulk samples do not show any signature related to the spin reorientation transition as it shows finite intensity for (1 0 0) reflection from 6 to 120 K (inset of Fig. 5). However, the magnetic data show a cusp around ∼42 K in the temperature-dependence curve. As the sample cools down to low temperature, the spin canting occurs, which results in the increase of magnetization, as shown in Fig. 4. Thus, the cusp observed around ∼42 K in the M-T data may be due to the spin canting effect. The Rietveld refined neutron-diffraction patterns at 300 K (paramagnetic state) and 3 K (magnetically ordered state) are shown in Fig. 6. Temperature variation of the lattice parameters, cell

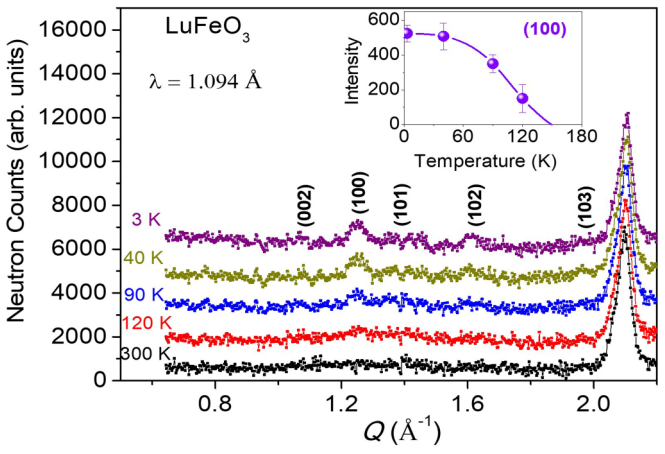

FIG. 5. The neutron-diffraction patterns for h-$LuFeO_3$ measured by PD-I ($\lambda = 1.094$ Å) at 3, 40, 90, 120, and 300 K. The inset shows the integrated intensity of the (100) magnetic Bragg peak as a function of temperature. The solid line in the inset is a guide to the eye.

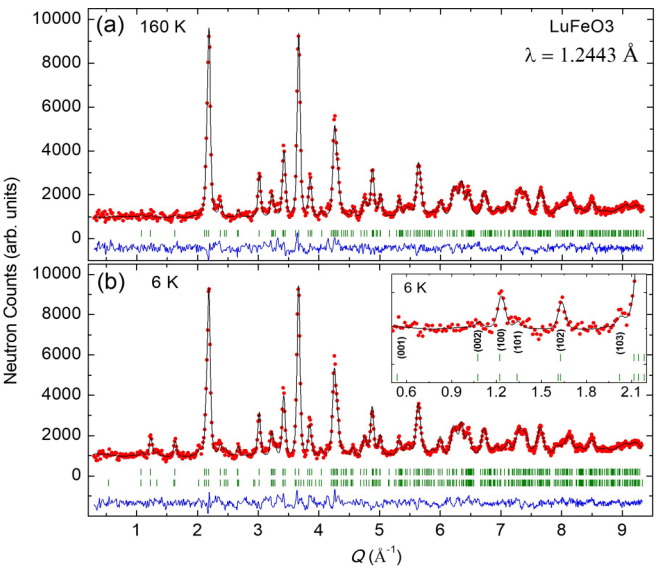

FIG. 6. Experimentally observed (circles) and calculated (solid lines through the data points) neutron-diffraction patterns for h-$LuFeO_3$ at (a) 160 K (paramagnetic state) and (b) 6 K (magnetically ordered state), respectively measured by PD-II ($\lambda = 1.249$ Å). The solid lines at the bottom of each panel represent the difference between observed and calculated patterns. The vertical bars indicate the positions of allowed nuclear and magnetic [the bottom row in (b)] Bragg peaks. The inset of (b) shows the zoomed pattern at 6 K over the low-Q range.

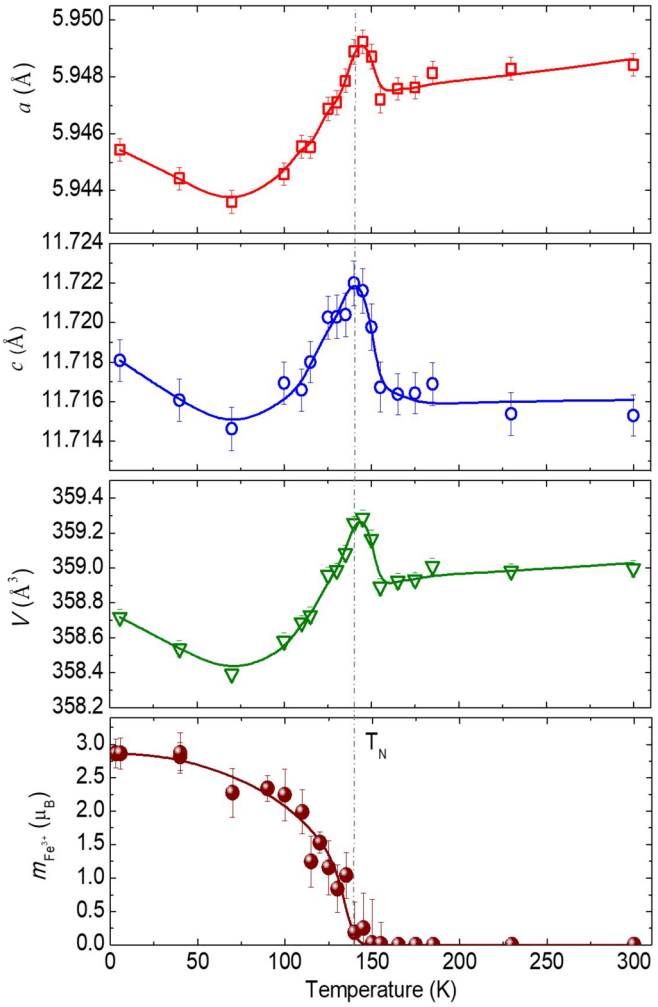

FIG. 7. Temperature variations of the lattice parameters (a), (c), the unit-cell volume (V), and the ordered magnetic moment of the Fe^{3+} ion for h-$LuFeO_3$. The solid lines are a guide to the eye.

volume, and ordered magnetic moment of the Fe^{3+} ion for $LuFeO_3$ are shown in Fig. 7. An anomaly in the temperature-dependent lattice constants has been found at T_N indicating a magnetoelastic coupling in $LuFeO_3$.

All the magnetic peaks could be indexed with a propagation vector $k = (0\,0\,0)$ with respect to the hexagonal nuclear unit cell. The symmetry-allowed magnetic structure is determined by a representation analysis using the program BASIREPS available within the FULLPROF suite [31]. The symmetry analysis reveals that there are six irreducible representations (IRs), i.e., six possible symmetry allowed magnetic structures. Among them, four IRs (Γ_1 to Γ_4) are one dimensional and two IRs (Γ_5 and Γ_6) are two dimensional. It is known that for isostructural hexagonal manganites only four one-dimensional IRs are required to describe the magnetic structures [18]. For each of these representations, the Fe sublattice displays antiferromagnetic order within the ab plane, forming 120° structures among the three spins in the triangular sublattice. For the homometric pairs, Γ_1 (Γ_2) and Γ_3 (Γ_4), one-dimensional IRs are found to be indistinguishable with perfectly identical neutron-scattering structure factors for our samples. Moreover,

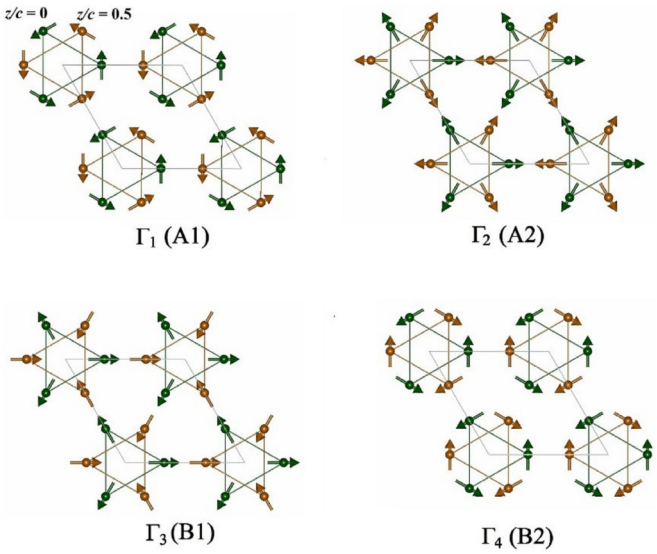

FIG. 8. The noncollinear spin patterns (Γ_1–Γ_4) are represented at $z = 0$ and $\frac{1}{2}$ along the z axis. The color variation is to differentiate the atoms.

the Γ_1 (Γ_3) and Γ_2 (Γ_4) are related by the in-plane rotations [17]. In the present paper, the highest and second highest magnetic intensity are found for the Bragg peaks (100) and (102), respectively. Among the four IRs, Γ_1 and Γ_3 magnetic structures contribute mainly to the (100) magnetic Bragg peak. For the Γ_2 and Γ_4 magnetic structures, the contributions to diffraction intensities from the Fe^{3+} sites of the $z = 1/2$ and 0 layers are canceled out for the (100) magnetic Bragg peak. The main contribution from Γ_2 and Γ_4 magnetic structures appears for the (101) magnetic Bragg peak. On the other hand, for the (102) peak, the diffraction intensity is nonzero for all the spin structures Γ_1 to Γ_4. Therefore, the magnetic structure of the present compound can be defined by either Γ_1 or Γ_3. The refinement with Γ_1 is shown in Fig. 6(b). A good agreement between observed and calculated pattern is evident. The corresponding magnetic structure is shown in Fig. 8. The magnetic structure is pure antiferromagnetic in nature without having any net magnetization per unit cell. The ordered site moment of Fe ions is found to be $m = 2.84(7)\,\mu_B/Fe^{3+}$ at 6 K (Fig. 7). Among the four IRs, only the Γ_2 allows for a ferromagnetic component along the c axis. A trial refinement with $\Gamma_1 + \Gamma_2$ results in a similar quality of fit for a finite moment component along the c axis (m_c) up to a maximum value of 0.4 μ_B. Therefore, if the ferromagnetic moment for our sample is present, it is significantly weak and the corresponding ordered moment (m_c) should be below 0.4 μ_B per Fe^{3+}.

The electrical properties of h-$LuFeO_3$ are investigated in the capacitor geometry. Figure 9 shows the frequency dependence of dielectric constant (ε') and loss measured at RT for h-$LuFeO_3$. The dielectric constant [see Fig. 9(a)] is large in the low-frequency region and decays exponentially as the frequency increases. The value of the dielectric constant decreases from 3000 at 100 Hz to 300 at 1 kHz showing a Debye-like relaxation. On the other hand, dielectric loss ($\tan\delta$) has a significantly high value at low frequencies, and the value reduces as the frequency increases to 10 kHz. Beyond 10 kHz,

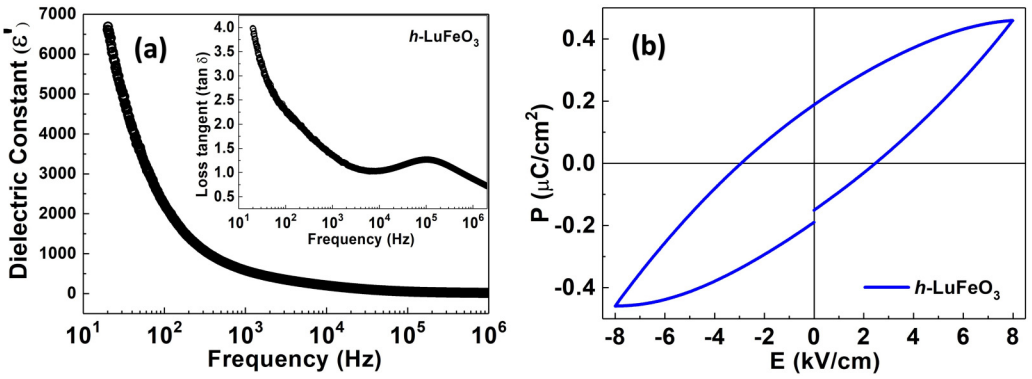

FIG. 9. (a) Dielectric constant versus frequency plot of h-$LuFeO_3$. The inset shows the loss tangent versus frequency. (b) P-E loop of h-$LuFeO_3$ ceramics.

loss again increases, having a peak around 100 kHz, and then decreases further with increasing frequency value.

Hexagonal ferrites exist in a polar $P6_3cm$ structure below the Curie temperature ($T_C \sim 1050$ K), while they possess the paraelectric $P6_3/mmc$ phase above the T_C. Hexagonal $LuFeO_3$, similar to manganites, is an improper ferroelectric, where induced polarization is nonlinearly coupled to the trimerization of rare-earth planes [12,49]. Below the Curie temperature, the size mismatch between the Lu^{3+} ion (small radius) and FeO_5 bipyramid (large radius) leads to an inward tilting of the FeO_5 polyhedra which is associated with a two-up/one-down buckling of the Lu planes (Fig. 1) [48,49]. This is called trimerization of the unit cell due to which the crystal attains the lower structural symmetry, $P6_3cm$. In this polar state, the strong asymmetric covalent bonding interaction between Lu and O along the c axis favors the off centering electric dipoles, eventually inducing ferroelectricity [26]. Since the magnetic transition is much below room temperature, the observed polarization is purely from the hexagonal structure.

The relative atomic positions in the lattice will experience a displacement when the structure changes from non-polar $P6_3/mmc$ to the polar $P6_3cm$ phase. These displacements can generally be represented in terms of K_1, K_3, and Γ_{2-} phonon modes, where K_1 and K_3 are the zone-boundary modes and Γ_{2-} is the zone-center polar mode [12,20]. The K_1 mode describes the Fe and O displacements in the ab plane, while the K_3 mode relates to the rotation of the FeO_5 bipyramids and buckling of the Lu-O planes [20]. Thus, the net polarization is induced as a result of the nonlinear coupling between K_3 and Γ_{2-} modes. The magnitude of K_1, K_3, and Γ_{2-} phonon modes is calculated based on the atomic positions at 300 K (Table I). The polarization values are estimated analytically from the atomic displacements (Δz), relative to respective positions in the undistorted $P6_3/mmc$ paraelectric phase by $P_s = (258 \pm 9) \times \Delta z\ \mu C/cm^2$ [50]. The resultant displacement amplitudes and the polarization values calculated using different methods are listed in Table III. The corresponding atomic pattern is shown in Fig. 10.

The P-E loop measured at room temperature is shown in Fig. 9(b). For applied electric field of 8 kV/cm, the observed electric coercivity is 2.71 kV, remnant polarization is $P_r \sim 0.18\ \mu C/cm^2$, and polarization is $P_{max} \sim 0.46\ \mu C/cm^2$ at an applied electric field, 8 kV/cm. The P-E loop appears more like a lossy dielectric loop, rather than an actual ferroelectric hysteresis loop [51]. The current conduction due to the mixed valance of Fe (Fe^{2+}/Fe^{3+}) or due to the oxygen vacancies results in such lossy loops in the h-$LuFeO_3$ system. Since the XPS data clearly show the Fe^{3+} state (Fig. 3), the presence of oxygen vacancies might lead to the lossy loops for the samples under study. In order to avoid the extrinsic contributions, the polarization measurements are performed using the Positive-Up Negative-Down (PUND) method [52] at 9-kV/cm applied electric field. The PUND results, which are intrinsic to the sample, are given as $P_{max} \sim 0.55\ \mu C/cm^2$ and $P_r \sim 0.04\ \mu C/cm^2$ (see Supplemental Material, Fig. S2 [44]). The ferroelectric polarization of h-$LuFeO_3$ has been calculated using the Berry-phase theory of polarization [53] for the crystal structure obtained from 6-K neutron-diffraction data, and is found to be $5.36\ \mu C/cm^2$. The ferroelectric polarization of h-$LuFeO_3$ is comparable with the $LuFe_{1-x}Mn_xO_3$ for $x = 0.25$ and is $3.4\ \mu C/cm^2$ [20]. Though the observed value is smaller than the theoretical predictions, it is much higher

TABLE II. Selective bond lengths and bond angles for h-$LuFeO_3$ at 300 K.

Bond lengths (Å)				Bond angles (°)	
Fe-O1	1.9361(2)	3 × Lu1/Lu2-O1	2.1839(2)/2.2017(2)	O1-Fe-O2	178.83(3)
Fe-O2	1.9772(2)	2 × Lu1/Lu2-O2	2.1613(2)/2.2822(1)	O1-Fe-O3	94.64(1)
Fe-O3	1.9664(2)	Lu1-O3	2.4597(3), 3.4211(5)	O1-Fe-O4	91.51(1)
Fe-O4	1.9987(2), 1.9984(1)	Lu2-O4	2.7031(3), 3.6784(4)	O2-Fe-O3	84.19(1)
				O2-Fe-O4	89.09(1)
				O3-Fe-O4	120.54(1)
				O4-Fe-O4	118.301(2)

TABLE III. Amplitude of the K_1, K_3, and Γ_{2-} phonon modes derived for the $P6_3/mmc$ to $P6_3cm$ distortion determined from the refined atomic positions at 300 K. The polarization is obtained from Ref. [49], as well DFT compared with experimental value.

	Phonon modes			$P(\mu C/cm^2)$		
Structure	K_1	K_3	Γ_{2-}	Analytical	DFT	Expt.
300 K (neutron)	0.091	0.8305	0.1414	7.88	5.36[a], 8.7 [55], 9 [21], 9.8 [12]	0.46
300 K (DFT)	0.0100	1.2538	0.2373	10.96		

[a]Present paper, calculations performed at 6 K.

compared to its orthorhombic phase, which has the polarization $\sim 7\,nC/cm^2$ [54]. In the case of the thin films, the value of the remnant polarization is reported to be $\sim 6.5\,\mu C/cm^2$ [26].

Temperature dependences of the heat capacity, dielectric constant, and derivative curve of susceptibility of h-$LuFeO_3$ below RT are shown in Fig. 11. From the dielectric data, it is noticed that the dielectric constant increases with increasing temperature with an anomaly at magnetic transition temperature, T_N. This is a characteristic of a coupling between ferroelectric and antiferromagnetic order, i.e., ME coupling, and such observations are also reported earlier for similar compounds [21,56]. The temperature-dependent specific heat curve (C_p/T versus T) also shows an anomaly at T_N which is consistent with the magnetic susceptibility data [$d\chi/dT$ in Fig. 11(c)]. In addition, the observed anomaly in the lattice parameters at T_N (Fig. 7) indicate a strong coupling between lattice-spin degrees of freedoms.

III. DENSITY FUNCTIONAL THEORY CALCULATIONS

The magnetic structure of h-$LuFO_3$ is an important discussion in recent years [12,18,26,49,57], because of its planar spin pattern among Fe atoms. The choice of planar spins for the Fe atom is strongly dependent on growth and stability of the sample phase. It is reported that a noncollinear planar triangular spin order is most preferable for h-$LuFeO_3$ [12,17,18,49] due to strong competing nearest-neighbor AFM interactions between Fe atoms. There are four fundamental planar spin patterns, namely, Γ_1, Γ_2, Γ_3, and Γ_4 (see Fig. 8), and combinations, i.e., $\Gamma_1 + \Gamma_2$ and $\Gamma_3 + \Gamma_4$, are possible for h-$LuFO_3$ [12,18,26,49]. In contrast to the results reported for thin films, i.e., a canted AFM structure (described by $\Gamma_1 + \Gamma_2$), our neutron-diffraction data reveal a pure in-plane antiferromagnetic spin structure (Γ_1) within the experimental error bar. This is where actual interest occurs to find the spin pattern through DFT calculations to understand the actual ground-state spin order for bulk h-$LuFeO_3$. We considered noncollinear spin calculations within spin-orbit coupling using Hubbard U and Hund's exchange parameter J_H, to relax the crystal and atomic structure at the experimental lattice parameters for neutron-diffraction data of h-$LuFeO_3$. We use norm-conserving pseudopotentials of Perdew-Burke-Ernzerhof exchange correlations [58]. All calculations are carried out using plane-wave pseudopotential density functional theory as implemented in QUANTUM ESPRESSO [59]. We use a k-point mesh of $8 \times 8 \times 4$ with electronic relaxation convergence to 1E-10Ry until the forces on the atom reduce to 1E-5Ry without any external constraints. Our noncollinear spin calculations of h-$LuFeO_3$ stabilized freely, without any constraint, and the optimized structural parameters are well reproduced as obtained in experiments (compared in Table I). From the DFT calculations, it is revealed that the noncollinear planar spin patterns are found to be lower in energy compared to the spin polarization along the z axis. As mentioned above, we have optimized the four fundamental planar spin patterns Γ_1, Γ_2, Γ_3, and Γ_4. We verified the ground-state spin order with different Hubbard U (= 4.0, 4.5, and 5.0 eV) and Hund's exchange parameter J_H (= 0.95, 1.00, and 1.05 eV). It is found that the ground state remains unchanged with the choice of U and J_H values (see Supplemental Material, Table S1 [44]); for consistency, further DFT calculations obtained using $U = 4.5$ eV with $J_H = 0.95$ eV are presented. It is found that the experimental lattice structure obtained from

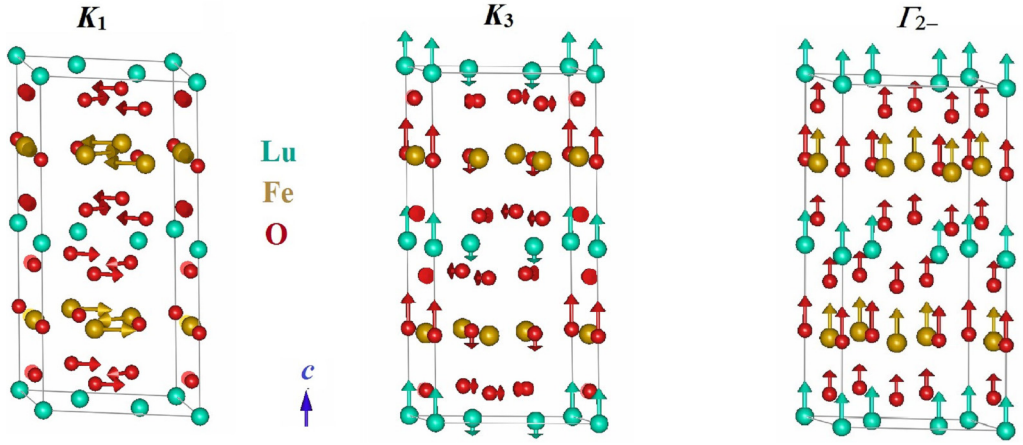

FIG. 10. The atomic pattern associated with the three phonon modes K_1, K_3, and Γ_{2-}, respectively.

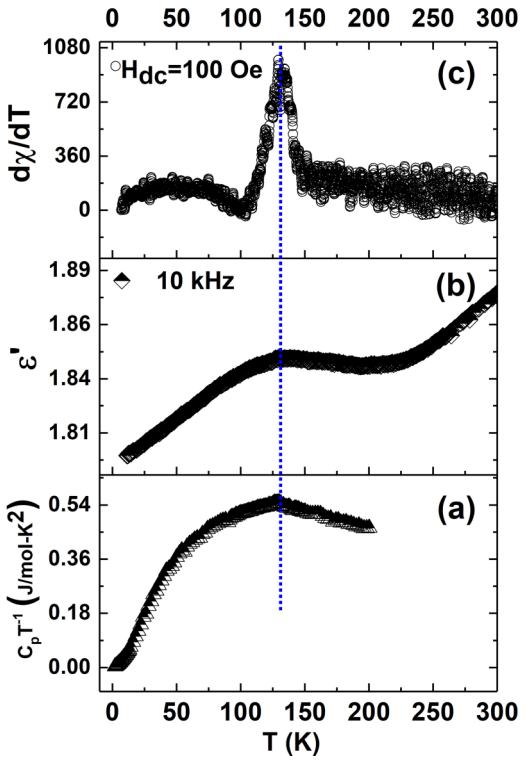

FIG. 11. Temperature dependence of (a) heat capacity, (b) dielectric constant, and (c) dc susceptibility of h-$LuFeO_3$ ceramics.

neutron-diffraction data at 6 K exhibits Γ_1 spin order as the ground state as shown in Fig. 8. The magnetic moments on Lu and O atoms have almost vanished to zero. The Γ_2 spin order with 0.010-meV/Fe higher energy is almost degenerate with Γ_1 spin order, whereas the Γ_3 and Γ_4 spin orders are with 0.011- and 0.056-meV/Fe higher energy compared to Γ_1 spin order. It is shown that the ground-state Γ_1 spin order has a clear energy difference compared to the Γ_2, Γ_3, and Γ_4 spin order for the obtained experimental crystal structure. Furthermore, the calculated m_z magnetic moment along the z axis for Fe atoms is found to be zero for the ground-state Γ_1 spin order.

Meanwhile, our neutron data and DFT calculations confirm that the spin pattern for bulk h-$LuFeO_3$ samples is associated to Γ_1. The experimental determined planar spin pattern for thin films [17,18,26] always acquires the substrate strains, and the spin pattern has a direct effect on the substrate in layered structures like h-$LuFeO_3$. In the case of bulk h-$LuFeO_3$, the Fe atoms have free choice of planar spin pattern. Furthermore, Hund's parameter (J_H) that represented h-$LuFeO_3$ thin films [12,49] leads to spin pattern Γ_2, but for bulk samples it leads to the Γ_1 spin pattern. Therefore, it is clear that the choice of planar spin pattern among Γ_1, Γ_2, Γ_3, and Γ_4 or their combinations ($\Gamma_1 + \Gamma_2, \Gamma_3 + \Gamma_4$) in h-$LuFeO_3$ is purely dependent on the sample architecture.

The electronic band structure and density of states for noncollinear h-$LuFeO_3$ are shown in Fig. 12. It has a wide band gap of 1.38 eV along M-Γ, while the reported band gap for thin films is 1.1 eV [12,49]. We see a clear variation in the electronic structure in the bulk compared to the thin films. From density of states, the states just below the Fermi level are from the Fe-3d and O-2p states, and the states between -0.5 and -2.5 eV are dominated by Lu-4f and O-2p states; however, there are smaller contributions from Lu-3d and Fe-3d states. The states between -2.5 to -6.5 eV are mainly due to the Fe-3s, Fe-3d, and O-2p states. The conduction band mainly contains the Fe-3d state near the Fermi level and Lu-3d at the higher-energy state.

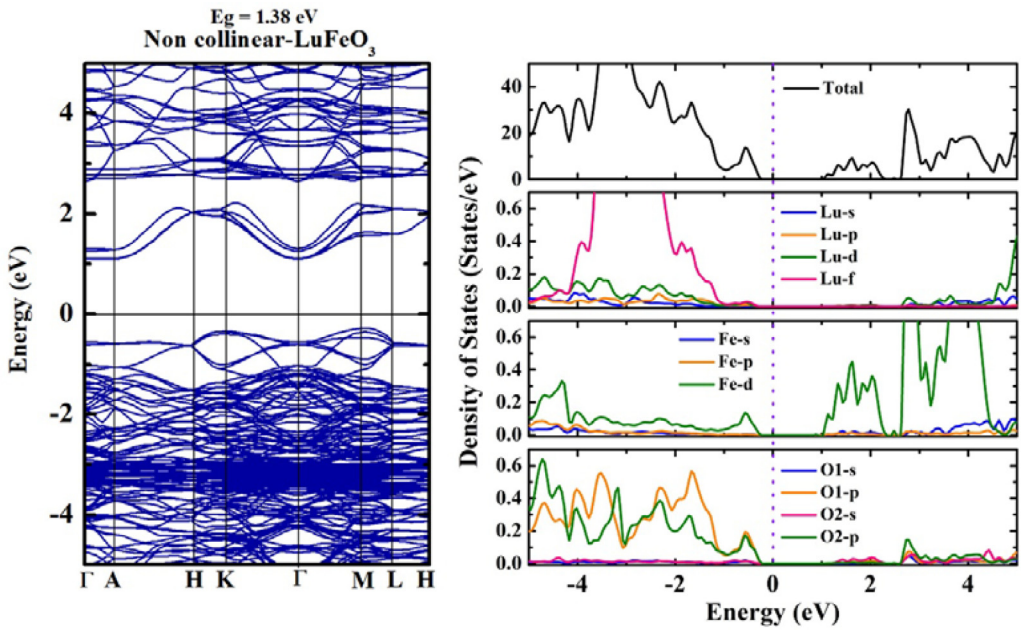

FIG. 12. The noncollinear band structure and density of states of h-$LuFeO_3$ calculated under spin-orbit coupling with $U = 4.5$ eV and $J_H = 0.95$ eV. The Fermi level is set to zero.

IV. CONCLUSIONS

We have successfully stabilized single phase hexagonal $LuFeO_3$ ceramics in bulk form using the sol-gel method and investigated the structural, electric, and magnetic properties of the h-$LuFeO_3$ bulk sample. The hexagonal crystal structure is confirmed by XRD and neutron diffraction, and supported by the corresponding Raman modes. XPS measurements show the Fe^{3+} valance state. The detailed neutron and magnetic measurements confirm the antiferromagnetic ordering (T_N) of hexagonal $LuFeO_3$ is at ∼130 K. Temperature-dependent magnetization curves show an additional anomaly at around ∼42 K may be due to a spin canting. At room temperature, the samples exhibit the paramagnetic state while a weak ferromagnetic nature is found at low temperatures due to the spin canting. Neutron data and DFT calculations reveal that the possible spin configuration of h-$LuFeO_3$ is associated with Γ_1 corresponding to a noncollinear 120° AFM spin structure. The 120° antiferromagnetic ordering is further confirmed with spin-orbit coupling density functional theory calculations. The on-site coulomb interaction (U) and Hund's parameter (J_H) on Fe atoms reproduced the neutron-diffraction Γ_1 spin pattern among the Fe atoms. Furthermore, Hund's parameter (J_H) that represented h-$LuFeO_3$ thin films leads to spin pattern Γ_2, while we have Γ_1 spin configuration for the bulk structure. An intrinsic ferroelectric polarization is observed at room temperature with remnant polarization $P_r \sim 0.18\,\mu C/cm^2$ and at an applied electric field, 8 kV/cm. An evidence of magnetoelectric coupling is found from dielectric, specific-heat measurements as they exhibit an anomaly at the magnetic transition temperature. Presence of a strong magnetoelastic coupling is confirmed from the variation of lattice parameters at T_N. This makes the material a fascinating candidate for fundamental physics and also promising from a practical application point of view.

ACKNOWLEDGMENTS

P.S. acknowledges financial support from University Grants Commission (UGC), India for the Dr. D. S. Kothari post-doctoral fellowship No. F.4-2/2006 (BSR)/PH/13-14/0085. The authors also acknowledge Centre for Nano Science and Engineering (CeNSE), Indian Institute of Science, Bengaluru. Computations were carried out using the resources provided by the Texas Advanced Computing Center. This project was supported financially by National Research Foundation of Korea Grants No. NRF-2017R1D1A1B03035932 (B.L.C.) and No. NRF-2016R1A2B4010105 (J.J.).

[1] J. F. Scott, Nat. Mater. **6**, 256 (2007).
[2] S.-W. Cheong and M. Mostovoy, Nat. Mater. **6**, 13 (2007).
[3] R. O. Cherifi, V. Ivanovskaya, L. C. Phillips, A. Zobelli, I. C. Infante, E. Jacquet, V. Garcia, S. Fusil, P. R. Briddon, N. Guiblin, A. Mougin, A. A. Unal, F. Kronast, S. Valencia, B. Dkhil, A. Barthélémy, and M. Bibes, Nat. Mater. **13**, 345 (2014).
[4] J. Wang, J. B. Neaton, H. Zheng, V. Nagarajan, S. B. Ogale, B. Liu, D. Viehland, V. Vaithyanathan, D. G. Schlom, U. V. Waghmare, N. A. Spaldin, K. M. Rabe, M. Wuttig, and R. Ramesh, Science **299**, 1719 (2003).
[5] M. Tachibana, T. Shimoyama, H. Kawaji, T. Atake, and E. Takayama-Muromachi, Phys. Rev. B **75**, 144425 (2007).
[6] H. L. Yakel, E. F. Forrat, E. F. Bertaut, and W. C. Koehler, Acta Crystallogr. **16**, 957 (1963).
[7] H. Katsura, N. Nagaosa, and A. V. Balatsky, Phys. Rev. Lett. **95**, 057205 (2005).
[8] S. Song, H. Han, H. M. Jang, Y. T. Kim, N.-S. Lee, C. G. Park, J. R. Kim, T. W. Noh, and J. F. Scott, Adv. Mater. **28**, 7430 (2016).
[9] B. Lorenz, ISRN Condens. Matter Phys. **2013**, 497073 (2013).
[10] A. Kumar, S. M. Yusuf, and C. Ritter, Phys. Rev. B **96**, 014427 (2017).
[11] M. Lilienblum, T. Lottermoser, S. Manz, S. M. Selbach, A. Cano, and M. Fiebig, Nature Phys. **11**, 1070 (2015).
[12] H. Das, A. L. Wysocki, Y. Geng, W. Wu, and C. J. Fennie, Nat. Comm. **5**, 2998 (2014).
[13] S. Lee, F. Gozzo, A. Pirogov, M. Kang, K.-H. Jang, M. Yonemura, T. Kamiyama, S.-W. Cheong, N. Shin, H. Kimura, Y. Noda, and J.-G. Park, Nature Letters **451**, 805 (2008).
[14] M. Fiebig, T. Lottermoser, and R.V. Pisarev, J. Appl. Phys. **93**, 8194 (2003).
[15] P. Tong, D. Louca, N. Lee, and S.-W. Cheong, Phys. Rev. B **86**, 094419 (2012).
[16] A. R. Akbashev, A. S. Semisalova, N. S. Perov, and A. R. Kaul, Appl. Phys. Lett. **99**, 122502 (2011).
[17] W. Wang, J. Zhao, W. Wang, Z. Gai, N. Balke, M. Chi, H. N. Lee, W. Tian, L. Zhu, X. Cheng, D. J. Keavney, J. Yi, T. Z. Ward, P. C. Snijders, H. M. Christen, W. Wu, J. Shen, and X. Xu, Phys. Rev. Lett. **110**, 237601 (2013).
[18] S. M. Disseler, J. A. Borchers, C. M. Brooks, J. A. Mundy, J. A. Moyer, D. A. Hillsberry, E. L. Thies, D. A. Tenne, J. Heron, M. E. Holtz, J. D. Clarkson, G. M. Stiehl, P. Schiffer, D. A. Muller, D. G. Schlom, and W. D. Ratcliff, Phys. Rev. Lett. **114**, 217602 (2015).
[19] M. L. Plumer and A. Caillé, J. Appl. Phys. **70**, 5961 (1991).
[20] S. M. Disseler, X. Luo, B. Gao, Y. S. Oh, R. Hu, Y. Wang, D. Quintana, A. Zhang, Q. Huang, J. Lau, R. Paul, J. W. Lynn, S-W. Cheong, and W. Ratcliff II, Phys. Rev. B **92**, 054435 (2015).
[21] L. Lin, H. M. Zhang, M. F. Liu, Shoudong Shen, S. Zhou, D. Li, X. Wang, Z. B. Yan, Z. D. Zhang, Jun Zhao, Shuai Dong, and J.-M. Liu, Phys. Rev. B **93**, 075146 (2016).
[22] R. L. White, J. Appl. Phys. **40**, 1061 (1964).
[23] X. S. Xu and W. B. Wang, Mod Phys. Lett. B **28**, 1430008 (2014).
[24] A. A. Bossak, I. E. Graboy, O. Y. Gorbenko, A. R. Kaul, M. S. Kartavtseva, V. L. Svetchnikov, and H. W. Zandbergen, Chem. Mater. **16**, 1751 (2004).
[25] S. Cao, X. Zhang, T. R. Paudel, K. Sinha, X. Wang, X. Jiang, W. Wang, S. Brutsche, J. Wang, P.J. Ryan, J-W. Kim, X. Cheng, E.Y. Tsymbal, P.A. Dowben, and X. Xu, J. Phys. Condens. Matter. **28**, 156001 (2016).
[26] Y. K. Jeong, J.-H. Lee, S.-J. Ahn, and H. M. Jang, Chem. Mater. **24**, 2426 (2012).
[27] M. S. V Kumar, K. Nagashio, T. Hibiya, and K. Kuribayashi, J. Am. Ceram. Soc. **91**, 806 (2008).
[28] M. S. V Kumar, K. Kuribayashi, and K. Kitazono, J. Am. Ceram. Soc. **92**, 903 (2009).

[29] E. Magome, C. Moriyoshi, Y. Kuroiwa, A. Masuno, and H. Inoue, Jap. Jour. Appl. Phys. **49**, 09ME06 (2010).
[30] A. Masuno, A. Ishimoto, C. Moriyoshi, N. Hayashi, H. Kawaji, Y. Kuroiwa, and H. Inoue, Inorg. Chem. **52**, 11889 (2013).
[31] FULLPROF suite, http://www.ill.eu/sites/fullprof/.
[32] K. Momma and F. Izumi, J. Appl. Crystallogr. **44**, 1272 (2011).
[33] Y. K. Jeong, J.-H. Lee, S.-J. Ahn, S.-W. Song, H. M. Jang, H. Choi, and J. F. Scott, J. Am. Chem. Soc. **134**, 1450 (2012).
[34] M. Cazayous, D. Malka, D. Lebeugle, and D. Colson, Appl. Phys. Lett. **91**, 071910 (2007).
[35] S. Venugopalan and M. M. Becker, J. Chem. Phys. **93**, 3833 (1990).
[36] M. N. Iliev, H. G. Lee, V. N. Popov, M. V. Abrashev, A. Hamed, R. L. Meng, and C. W. Chu, Phys. Rev. B **56**, 2488 (1997).
[37] A. Ghosh, J. R. Sahu, S. V. Bhat, and C. N. R. Rao, Solid State Sci. **11**, 1639 (2009).
[38] L. P. Zhu, H. M. Deng, L. Sun, J. Yang, P. X. Yang, and J. H. Chu, Cer. International. **40**, 1171 (2014).
[39] A. P. Grosvenor, B. A. Kobe, M. C. Biesinger, and N. S. McIntyre, Surf. Interface Anal. **36**, 1564 (2004).
[40] J. A. Kurzman, J. Li, T. D. Schladt, C. R. Parra, X. Y. Ouyang, R. Davis, J. T. Miller, S. L. Scott, and R. Seshadri, Inorg. Chem. **50**, 8073 (2011).
[41] F. Liu, J. Li, Q. Li, Y. Wang, X. Zhao, Y. Hua, C. Wang and X. Liu, Dalton Trans. **43**, 1691 (2014).
[42] L. Yin, I. Adler, T. Tsang, L. J. Matienzo, and S. O. Grim, Chem. Phys. Lett. **24**, 81 (1974).
[43] Z. Fu, H. S. Nair, Y. Xiao, A. Senyshyn, V. Y. Pomjakushin, E. Feng, Y. Su, W. T. Jin, and T. Bruckel, Phys. Rev. B **94**, 125150 (2016).
[44] See Supplemental Material at http://link.aps.org/supplemental/10.1103/PhysRevB.97.184419 for the field cooled curve of h-$LuFeO_3$ at an applied field of 1 kOe and the Curie-Weiss fit of the FC data. The PUND polarization measurement of the h-$LuFeO_3$ sample at 9 kV/cm applied electric field, along with the total-energy difference (meV/Fe) compared from the ground state (Γ_1) to the Γ_2, Γ_3, and Γ_4 spin configuration with diiferent choice of Hubbard U (4.0, 4.5, and 5.0 eV) with Hund's J_H (0.95, 1.00, and 1.05 eV).
[45] H. J. Lewtas, A. T. Boothroyd, M. Rotter, D. Prabhakaran, H. Muller, M. D. Le, B. Roessli, J. Gavilano, and P. Bourges, Phys. Rev. B **82**, 184420 (2010).
[46] H. S. Nair, Z. Fu, C. M. N. Kumar, V. Y. Pomjakushin, Y. Xiao, T. Chatterji, and A. M. Strydom, Euro. Phys. Lett. **110**, 37007 (2015).
[47] T. Katsufuji, M. Masaki, A. Machida, M. Moritomo, K. Kato, E. Nishibori, M. Takata, M. Sakata, K. Ohoyama, K. Kitazawa, and H. Takagi, Phys. Rev. B **66**, 134434 (2002).
[48] M. Ye and D. Vanderbilt, Phys. Rev. B **92**, 035107 (2015).
[49] H. Wang, I. V. Solovyev, W. Wang, X. Wang, P. J. Ryan, D. J. Keavney, J.-W. Kim, T. Z. Ward, L. Zhu, J. Shen, X. M. Cheng, L. He, X. Xu, and X. Wu, Phys. Rev. B **90**, 014436 (2014).
[50] S. C. Abrahams, S. K. Kurtz, and P. B. Jamieson, Phys. Rev. **172**551 (1968)
[51] J. F. Scott, J. Phys.: Condens. Matter **20**, 021001 (2008).
[52] S. M. Feng, Y. S. Chai, J. L. Zhu, N. Manivannan, Y. S. Oh, L. J. Wang, Y. S. Yang, C. Q. Jin, and Kee Hoon Kim, New J. Phys. **12**, 073006 (2010).
[53] R. D. King-Smith and D. Vanderbilt, Phys. Rev. B **47**, 1651 (1993).
[54] U. Chowdhury, S. Goswami, D. Bhattacharya, J. Ghosh, S. Basu, and S. Neogi, Appl. Phys. Lett. **105**, 052911 (2014).
[55] Ch. Xu, Y. Yang, S. Wang, W. Duan, B. Gu, and L. Bellaiche, Phys. Rev. B **89**, 205122 (2014).
[56] D. G. Tomuta, S. Ramakrishnan, G. J. Nieuwenhuys, and J. A. Mydosh, J. Phys.: Condens. Matter. **13**, 4543 (2001).
[57] B. S. Holinsworth, D. Mazumdar, C. M. Brooks, J. A. Mundy, H. Das, J. G. Cherian1, S. A. McGill, C. J. Fennie, D. G. Schlom, and J. L. Musfeldt, App. Phys. Lett. **106**, 082902 (2015).
[58] J. P. Perdew, K. Burke, and M. Ernzerhof, Phys. Rev. Lett. **77**, 3865 (1996).
[59] P. Giannozzi, S. Baroni, N. Bonini, M. Calandra, R. Car, C. Cavazzoni, D. Ceresoli, G. L. Chiarotti, M. Cococcioni, I. Dabo, A. D. Corso, S. de Gironcoli, S. Fabris, G. Fratesi, R. Gebauer, U. Gerstmann, C. Gougoussis, A. Kokalj, M. Lazzeri, L. Martin-Samos, N. Marzari, F. Mauri, R. Mazzarello, S. Paolini, A. Pasquarello, L. Paulatto, C. Sbraccia, S. Scandolo, G. Sclauzero, A. P. Seitsonen, A. Smogunov, P. Umari, and R. M. Wentzcovitch, J. Phys.: Condens. Matter **21**, 395502 (2009).